Electronic Supplementary Material

Unrevealing the opto-structural features of luminescent polymeric films containing Eu^{III}-doped phosphors through spectroscopic and theoretical perspectives

Leonardo F. Saraiva,[a,b] Airton G. Bispo-Jr,[c] Sergio A. M. Lima,[a,b] Ana M. Pires*[a,b]

[a] São Paulo State University (Unesp), School of Technology and Sciences, Presidente Prudente, SP, Brazil. [b] São Paulo State University (Unesp), Institute of Biosciences, Humanities and Exact Sciences, São José do Rio Preto-SP, Brazil. [c] University of Campinas (UNICAMP), Institute of Chemistry, Campinas, SP, Brazil.

Table of contents

Supplementary Note S1 – Film characterization

X-ray diffraction (XRD). XRD patterns of the phosphor and films were recorded using a SIEMENS diffractometer model D5000, Cu Kα radiation (λ = 1.4505 Å) within the 10–80° range (step of 0.02) at accelerating voltage of 30 kV and integration time of 0.1 s. The measurement was performed at room temperature (298 K).

Thermogravimetric analysis (TGA). The analyses were carried using TA instruments equipment (model SDT Q600), from an approximate weight of 4 mg of each sample in an alumina crucible under purified nitrogen gas flux (15 mL min^{-1}) and a heating rate of 10 °C/min from 25 °C to 1000 °C.

FTIR and Raman spectroscopy. Fourier-transform infrared spectroscopy (FTIR) was recorded in a Perkin Elmer Frontier spectrometer through the diamond attenuated total reflection (ATR) mode within the 250 – 4000 cm^{-1} spectral range and increment of 2 cm^{-1}. Raman spectra at room temperature were measured using a 633 nm laser at a micro-Raman Renishaw spectrograph, in Via-model, equipped with a Leica optical microscope and CCD PELTIER detector. Also, the presence of a dichroic mirror situated in front of the spectrograph was set to reduce the transmitted excitation beam, which affects the intensity of the bands near the laser excitation wavelength (633 nm).

SEM. The scanning electron microscopy (SEM) was carried on a Hitachi model SU3800 scanning-electron microscope with a detector of secondary and backscattering electrons in a high vacuum and at a constant temperature. The films were previously coated with a thin gold layer by using a sputtering QUORUM, Q 150R ES model.

TEM. Transmission electron microscopy (TEM) was carried out in a JEOL model JEM-2100 equipped with an energy dispersive spectroscopy (EDS). The samples were dispersed in ethanol; the one drop of solution was dispersed in a carbon coated copper backing. The analysis was performed at room temperature (298 K) after drying samples.

Confocal microscopy. The confocal measurements of the films were done in a Nikon Confocal Microscope model C2/C2si with an advanced inverted microscope system (Eclipse Ti-E), at a magnification of ×20, by using a laser channel of 405 nm (DAPI channel).

Diffuse reflectance spectroscopy. Diffuse reflectance spectra (DRS) in the UV-Vis region were accomplished by using a spectrometer Cary 500 Scan model. The optical band gap values were evaluated from the diffuse reflectance data straight from a graphic of $(\alpha hv)^n$ versus the energy of the incident photon in eV (hv), where *n* has a value equal to 2 for direct gap transitions in SrY_2O_4[1]. The ratio of the absorption (*S*) and the scattering (*K*) coefficients gives the α constant, calculated according to the Kubelka-Munk's approximation (equation S1)[2,3], where *R* is the reflectance observed for different incident energies, and the optical bandgap value is obtained from the extrapolation of the curve to the zero-ordinate value.

$$\alpha = \frac{K}{S} = \frac{(1-R)^2}{2R} \quad (S1)$$

Refractive index determination. The correct value of refractive index is essential in determining the photophysical parameters of all samples. Under this circumstance, two approximations for calculating the refractive index were tested (equation S2 and equation S3). In approximation (1), α is the absorption coefficient and λ_e is the absorption edge wavelength. In approximation (2), E_g is the energy of the optical bandgap in eV. The obtained values were summarized in Table S1.

$$n = 1 + \frac{1}{2\pi^2}\int \frac{\alpha}{1-\left(\frac{\lambda}{\lambda_e}\right)^2} d\lambda \quad (S1)$$

$$1 - \frac{n^2-1}{n^2+1} = \left(\frac{E_g}{20}\right)^{1/2} \quad (S2)$$

Table S1. Values of refractive index determined by using each approximation.

Film / %	Approximation 1	Approximation 2
40	1.506	1.564
45	1.515	1.590
50	1.528	1.612
55	1.531	1.624
60	1.539	1.631
65	1.554	1.642
70	1.568	1.671

Among these results, we consider approximation 1 more well-suited for the photophysical analysis, as we have considered the wavelength while it was neglected in approximation 2.

Steady-state and time-resolved luminescence. Photoluminescence excitation and emission spectra at (298 K, excitation, and emission band pass of 0.5 nm) were performed in a Horiba Jobin Yvon spectrometer Fluorog model FL3–222 with a Xe lamp (450 W) source with a double excitation monochromator with the corrected intensity of the Xe lamp excitation, and the signal detection. Emission decay curves were carried out in a phosphorimeter equipped with a Xe (5 J/pulse) lamp at 298 K. Samples were placed in support for solids and the measurements were carried out in front face mode.

Experimental photophysical analysis. The experimental Judd-Ofelt intensity parameters were calculated from the emission spectrum measured at 298 K applying equations (S4) and (S5), where *A* is the Einstein coefficient of spontaneous emission. In equation (S4), the term $I_{0\text{-}\lambda}$ is the area under the curve related to the $^5D_0 \rightarrow {}^7F_\lambda$ transition, $h\nu_{0-\lambda}$ is the energetic barycenter of the 0–λ. In equation (S5), the squared reduced matrix elements $\left\langle {}^7F_\lambda \middle\| U^{(\lambda)} \middle\| {}^5D_0 \right\rangle^2$ assume values of 0.0032 for Ω_2, and 0.0023 for Ω_4 [4], *e* is the electron charge, *c* is the speed of light, *h* and ε_0 are the Planck's and vacuum permittivity constants, respectively. Also, χ is the Lorentz Local field correction, given by the expression $n(n+2)^2/9$ and n is the refractive index of the medium ($n \approx 1.488$ considering PMMA refractive index at the orange-red wavelength region), and $\omega_{0-\lambda}$ is the angular frequency of the $^5D_0 \rightarrow {}^7F_\lambda$ (λ = 2, 4) emission[5]. In this work, Ω_6 was not considered since, in this model, it is derived from the $^5D_0 \rightarrow {}^7F_6$, which is out of the sensibility range in the fluorimeter.

$$A_{0-\lambda} = \frac{I_{0-\lambda}}{I_{0-1}} \frac{h\nu_{0-1}}{h\nu_{0-\lambda}} \quad (S4)$$

$$\Omega_\lambda^{exp} = \frac{3\hbar c^3 A_{0-\lambda}}{4e^2(\omega_{0-\lambda})^3 \chi \left\langle {}^7F_\lambda \middle\| U^{(\lambda)} \middle\| {}^5D_0 \right\rangle^2} \quad (S5)$$

The emission decay curves were monitored for all films, and the $^5D_0$ state lifetime was obtained with equation (S6), in which the parameters were extracted from a bi-exponential fit to estimate the intrinsic quantum yield. This property is defined in

equation (S7) as the ratio between the radiative (A_{rad}) and total contributions (radiative and non-radiative, A_{nrad}), where the A_{rad} is expressed in equation (S8) as a sum of each band component assigned to Eu^{3+} *f-f* transitions. Otherwise, the A_{nrad} values were calculated using equation (S9), where the inverse of the weighted average experimental $^5D_0$ state lifetime is taken into account. Also, the branching ratio was calculated with the area of the band attributable to the $^5D_0 \rightarrow {}^7F_2$ in the emission spectra, and the sum of the area of all bands related to the $^5D_0 \rightarrow {}^7F_{2\text{-}4}$ transitions (equation S10).

$$\langle \tau \rangle = \frac{\sum A_i \tau_i^2}{\sum A_i \tau_i} \quad (S6)$$

$$\Phi_{Eu}^{Eu} = \frac{A_{rad}}{A_{rad} + A_{nrad}} \quad (S7)$$

$$A_{rad} = \sum_J A_{0-J} \quad (S8)$$

$$A_{total} = \frac{1}{\langle \tau \rangle} = A_{rad} + A_{nrad} \quad (S9)$$

$$\beta_R(\psi(0), \psi(2)) = \frac{A(\psi(0), \psi(2))}{\sum_{J'=0-4} A(\psi(0), \psi J')} \quad (S10)$$

Supplementary Note S2 – Description of the tight-binding quantum-chemical model used in the composite optimization.

The computational modeling of materials at an atomistic level is an essential tool in today science and has become a vital element in the research available nowadays[6]. In this sense, in the last years, key properties such as interactions and vibrational frequencies are in high demand[7]. However, for systems with more than 1000 atoms, the obtention of these features from *ab-initio* calculations is practically impossible, increasing the necessity of new methods that are able to treat large systems. Thus, in this section, we will highlight the important characteristics of the GFN*n*-xTB software, whose focus is the vibrational and noncovalent interactions.

The GFN*n*-xTB consists of a minimal basis set of atoms centered, approximate Slater function as contractions of standard primitive Gaussian functions (STO-*m*G), augmented with a second *d*-polarization functions for heavy elements and *s*-function for hydrogen to enhance the accuracy of hydrogen bonding. Thus, the wavefunction choice in GFN*n*-xTB methods is described below in equation S11, where χ_z^μ is the primitive Gaussian type orbitals (GTOs) that contribute to the contracted GTO φ_μ, where $d_{z\mu}$ are the corresponding contraction coefficients[8]. The useful φ_μ is used in the expansion of the molecular orbitals through a linear combination with the orbital coefficient $C_{\mu j}$ (equation S12)[9]. The energies are found by the derivation of the expression as a function of the orbital coefficients, generating the Roothaan-Hall-type generalized eigenvalue equation S13[10,11]. Here, *C* is the matrix of orbital coefficients, *ε* is a diagonal matrix of orbital energies, *S* is the atomic orbital overlap matrix, and *F* is the xTB Hamiltonian matrix.

$$\varphi_\mu^{STO}(r) \approx \varphi_\mu(r) = \sum_z^{N_{prim}^\mu} d_{z\mu}\chi_z^\mu(r) \quad (S11)$$

$$\psi_j(r) = \sum_\mu^{N_{AO}} C_{\mu j}\varphi_\mu(r) \quad (S12)$$

$$FC = SC\varepsilon \quad (S13)$$

These wavefunctions may also be extended to comprise generalized periodic systems, where now ψ_j corresponds to a crystal orbital with the Bloch function equivalent for the one-particle functions (equation S14) with the Born-von-Kármán cyclic boundary conditions $\psi_j(\vec{r}+\vec{L},\vec{k}) = \psi_j(\vec{r},\vec{k})$[9]. The equation S14 can be expanded in the previous AOs, where the crystal orbitals are then expressed in equation S15, in which the summation relates over all N_L cells, related by the translation vector $\vec{L}$. We highlight that xTB implements the cyclic cluster model (CCM), considering the nearest neighbors $(N_L \rightarrow N_L^{CCM})$ with the corresponding weights for the Bloch function expansion[12]. This model supposes the vanishing of interaction beyond Wigner-Seitz cell, enabling the re-writing of Roothan-Hall-type equations for the crystal orbitals (equation S16).

$$\psi_j(\vec{r}+\vec{L},\vec{k}) = \psi_j(\vec{r},\vec{k}) exp\left[i\vec{k}\vec{L}\right] \quad (S14)$$

$$\psi_j(\vec{r},\vec{k}) = \sum_{\mu} C_{\mu j}(\vec{k}) \frac{1}{\sqrt{N_L}} \sum_{\vec{L}}^{N_L} \phi_{\mu}^{\vec{L}}(\vec{r})\, exp\left[i\vec{k}\vec{L}\right] \quad (S15)$$

$$\sum_{\vec{L}=\vec{0}}^{N_L^{CCM}} exp\left[i\vec{k}\vec{L}\right] \sum_{\mu} \left(F_{\mu\upsilon}^{\vec{0}\vec{L}} - \varepsilon_j(\vec{k}) S_{\mu\nu}^{\vec{0}\vec{L}}\right) C_{\mu j}(\vec{k}) w_{\mu\nu} = 0 \quad (S16)$$

In equation S16, the $F_{\mu\upsilon}^{\vec{0}\vec{L}}$ term represents the element of the Hamiltonian matrix, $\varepsilon_j(\vec{k})$ is the energy of the *j-th* crystal orbital, and the element of the overlap matrix is represented by $S_{\mu\nu}^{\vec{0}\vec{L}}$. Here, all calculations run over the high-symmetry Γ point in the Brillouin zone[12]. Therefore, in our optimization of the composite we restricted the treatment of the 2×2×2 supercell using the periodic boundary model adopted in xTB, while the first 300 atoms around the supercell were treated under the localized model described before, and the rest of the system was described through a self-parametrized force-field.

It is worth noting that the GFN2-xTB method[13] is the first off-the-shelf tight-binding method with multiple electrostatics, anisotropic exchange correlation (XC) contributions, and charge-dependent dispersion interactions (D4), where the total energy is described by equation S17[9], which was used to highlight the phosphor-polymer

interactions. In this equation, the superscript indicates the origin of the respective terms in the tight-binding expansion. The classical repulsion energy is denoted in equation S18, where Z^{eff} is the element-specific constants defining the magnitude for the repulsion energy. The extended Hückel energy (EHT) is ascribed in equation S19 since typical tight-binding methods allow the formation of covalent bond formation through EHT[14], where the valence electron density matrix in the nonorthogonal atomic orbitals is $P_{\mu\nu} = P^0_{\mu\nu} + \delta P_{\mu\nu}$, and the EHT matrix elements ($H^{EHT}_{\nu\mu}$) are detailed in equation S20. Here, $K^{ll'}_{AB}$ is an element pair-specific scaling parameter, $S_{\mu\nu}$ is the overlap matrix elements of the atomic orbitals ϕ_μ and ϕ_ν, and the diagonal matrix elements are $H_{\mu\mu}$ and $H_{\nu\nu}$, which depends on the chemical environment. Also, the isotropic electrostatic and XC energy originate from the second-order term in the tight-binding expansion (equation S21)[15,16,17,18] where $q_l/q_{l'}$ are partial Mulliken charges and $\gamma_{AB,ll'}$ are short-ranged damped Coulomb interactions (S22).

$$E_{GFN2-xTB} = E_{rep} + E^{D4'}_{disp} + E_{EHT} + E_\gamma + E_{AES} + E_{AXC} + E^{GFN2}_\Gamma \quad (S17)$$

$$E_{rep} = \frac{1}{2}\sum_{A,B} \frac{Z^{eff}_A Z^{eff}_B}{R_{AB}} e^{-\sqrt{\alpha_A \alpha_B}(R_{AB})^{kf}} \quad (S18)$$

$$E_{EHT} = \sum_{\mu\nu} P_{\mu\nu} H^{EHT}_{\nu\mu} \quad (S19)$$

$$H^{EHT}_{\nu\mu} = \frac{1}{2} K^{ll'}_{AB} S_{\mu\nu} \left(H_{\mu\mu} + H_{\nu\nu}\right) X(EN_A, EN_B) \Pi(R_{AB}, l, l') Y(\zeta^A_l, \zeta^B_{l'}) \quad (S20)$$

$$E_\gamma = \frac{1}{2} \sum_{A,B}^{N_{atoms}} \sum_{l \in A} \sum_{l' \in B} q_l q_{l'} \gamma_{AB,ll'} \quad (S21)$$

$$\gamma_{AB,ll'} = \frac{1}{\sqrt{R^2_{AB} + \eta^{-2}_{AB,ll'}}} \quad (S22)$$

In the used GFN2-xTB, the shell-exponent term, included in the description of the extended-Hückel model (EHT) is in detail in equation S23, where ζ^A_l are the Slater-type-orbitals (STO)[8] exponents of the GFN2-xTB atomic orbital basis. However, the EHT diagonal matrix elements are atomic environment-dependent (equation S24), in which h^l_A is a shell- and element-specific parameter.

$$Y(\zeta_l^A, \zeta_{l'}^B) = \left(\frac{2\sqrt{\zeta_l^A, \zeta_{l'}^B}}{\zeta_l^A + \zeta_{l'}^B}\right)^{\frac{1}{2}} \quad (S23)$$

$$H_{\kappa\kappa} = h_A^l - \delta h_{CN_A'}^l CN_A' \quad (S24)$$

Also, the dispersion energy denoted in equation S17 here is described by a modified model[19], detailed in equation S25, in which the three-body Axilrod-Teller-Muto (ATM) term is in the second line, while the third line describes the dependence of the two-body London dispersion energy, and the covalent coordination number CN_{cov}^A with the atomic charges q_A.

$$E_{disp}^{D4'} = -\sum_{A>B}\sum_{n=6,8} s_n \frac{C_n^{AB}(q_A, CN_{cov}^A, q_B, CN_{cov}^B)}{R_{AB}^n} f_{damp,BJ}^{(n)}(R_{AB}) - s_9 \sum_{A>B>C} \frac{(3\cos(\theta_{ABC})\cos(\theta_{BCA})\cos(\theta_{CAB}) + 1) C_9^{ABC}(CN_{cov}^A, CN_{cov}^B, CN_{cov}^C)}{(R_{AB}R_{AC}R_{BC})^3} \times f_{damp,zero}^{(9)}(R_{AB}, R_{AC}, R_{BC}) \quad (S25)$$

The anisotropic electrostatic and exchange correlation (XC) terms are written in the equation S26, where μ_A is the cumulative atomic dipole moment of atom A and the corresponding traceless of the quadrupole moment is Θ_A[20]. Finally, the second-order anisotropic XC energy is given by equation S27 in the case of GFN2-xTB.

$$E_{AES} = \frac{1}{2}\sum_{A,B}\{f_3(R_{AB})[q_A(\mu_B^T R_{BA}) + q_B(\mu_A^T R_{AB})] + f_5(R_{AB})[q_A R_{AB}^T \Theta_B R_{AB} + q_B R_{AB}^T \Theta_A R_{AB} - 3(\mu_A^T R_{AB})(\mu_B^T R_{AB}) + (\mu_A^T \mu_B) R_{AB}^2]\} \quad (S26)$$

$$E_{AXC} = \sum_A \left(f_{XC}^{\mu_A}|\mu_A|^2 + f_{XC}^{\Theta_A}\|\Theta_A\|^2\right) \quad (S27)$$

The lanthanides in this model were treated under the *f*-in-core approximation, in which they are treated as 4*d* transition metals with three valence electrons and no explicit consideration of the *f*-electrons. Previous ab initio calculation reported in the literature indicates that the *f*-electron shell lies below the valence shell, and they can be treated with an appropriate parametrization (GFN-xTB)[21], unless spectroscopic

properties are required, which is not the case here, since only structural and interaction properties are of interest.

Supplementary Note S3 – Procedure for the theoretical calculation of the Judd-Ofelt Intensity Parameters and the Force Constants

The calculation of the theoretical intensity parameter of lanthanides is quite common in the literature[22], however, this is the first time that they were applied to a phosphor/PMMA film. Therefore, in this section, we introduce important aspects of the formalism and adaptations proposed by us to perform an accurate calculation.

At first, we denote that these parameters are highly dependent on the chemical environment and the rare-earth ion, where the overall environment-dependent parameters $B_{\lambda tp}$ is a sum of the forced electric dipole (FED) and dynamic coupling (DC) contributions $\left(B_{\lambda tp}^{FED} + B_{\lambda tp}^{DC}\right)$, as detailed in equation S28, S29 and S30.

$$\Omega_{\lambda}^{theo} = (2\lambda + 1)\sum_{t,p}\frac{\left|B_{\lambda tp}\right|^2}{2t+1},\ B_{\lambda tp} = B_{\lambda tp}^{FED} + B_{\lambda tp}^{DC} \quad (S28)$$

$$B_{\lambda tp}^{FED} = \frac{2}{\Delta E}\langle r^{t+1}\rangle\Theta(t,\lambda)\left(\frac{4\pi}{2t+1}\right)^{1/2}\left(\sum_j e^2\rho_j g_j\left(2\beta_j\right)^{t+1}\frac{Y_{p,j}^{t*}}{R_j^{t+1}}\right) \quad (S29)$$

$$B_{\lambda tp}^{DC} = -\left[\frac{(\lambda+1)(2\lambda+3)}{(2\lambda+1)}\right]^{1/2}\langle r^{\lambda}\rangle\langle 3||C^{(\lambda)}||3\rangle\left(\frac{4\pi}{2t+1}\right)^{1/2} \times\left(\sum_j\left[\left(2B_j\right)^{t+1}\alpha_{OP,j} + \alpha_j'\right]\frac{Y_{p,j}^{t*}}{R_j^{t+1}}\right)\delta_{t,\lambda+1} \quad (S30)$$

Equation (S29) represents the contribution from the forced electric dipole (FED) through an adaptation of the original Judd-Ofelt theory by considering the charge factor (g) on the basis of the simple overlap model (SOM)[23]. Equation (S30) exhibits the expression for the dynamic coupling contribution (DC) within the scope of the bond overlap model (BOM)[24]. We emphasize that both models consider the covalency effects. In equation S29, ΔE is the energy difference between the barycenter of the excited $4f^{n-1}5d^1$ and ground $4f^n$ configurations, $\Theta(t,\lambda)$ are the numerical factors, defined as the relation between *f-g* and *f-d* interconfigurational transitions and 4*f* radial integrals, with

values of Θ(1,2) = –0.17, Θ(3,2) = 0.34, Θ(3,4) = 0.18, Θ(5,4) = –0.24, Θ(5,6) = –0.24, and Θ(7,6) = 0.24[25]. Also, g is the charge factor (equation S31), that combined with the overlap integral (ρ), composes the overlap charge between the Ln–L. The value of β parameter is given by $(1 \pm \rho)^{-1}$, whereas Y_p^{t*} is the conjugated spherical harmonics for l = 3, where the environment around the Ln^{3+} is treated by the sum over the *j-th* atom. The ligand polarizability is described in terms of the bond overlap polarizability and effective polarizability (α_{OP} and α', respectively). The first is commonly used to describe the covalency degree (equation S32), while the latter defines a specific molecular region that influences directly or indirectly the chemical environment of the lanthanide[24].

$$g_j = R_j \sqrt{\frac{k_j}{2\Delta\varepsilon_j}} \quad (S31)$$

$$\alpha_{OP} = \frac{e^2 {\rho_j}^2 R_j^2}{2\Delta\varepsilon_j} \quad (S32)$$

In our study, the effective polarizability of the *j-th* ligand (α_j') was determined through the fitting procedure in the *JoySpectra* platform[26] to minimize the residue between the experimental and theoretical parameters, and more information of the fitting method is described in reference [26]. Furthermore, the bond overlap polarizability was calculated extracting ρ_j and $\Delta\varepsilon_j$ from reference [27] using an exponential fit.

Regarding the calculation of the charge factors, the same values of $\Delta\varepsilon_j$ used in the α_{OP} can be applied, and as a consequence, only the k_j needs to be determined. For this purpose, previous work available in the literature reports a pseudo diatomic-like model[24] and local vibrational mode theory (LMV)[25] to calculate the k_j force constants (and corresponding g). However, these methods require *ab-initio* calculations or DFT-level computations to obtain the average weighted hessian matrix, which is impossible in our system due to the number of atoms and the long-range interactions between the Ln and the ligands in a first coordination sphere. Thus, the method we employed is detailed in the following.

In the case of a Ln^{3+} complex with monodentate organic ligands such as triphenylphosphine oxide, there is a direct effect of the bond stretch in the energy, since it is possible to check the energy variation while stretching the Ln–L bond [22]. Regarding

our study, the matter is more complicated for being an inorganic matrix, since the displacement of any ligand in a solid generates deviations in both Ln–L bond lengths of other bonds of the displaced ion, contributing effectively to the obtained *k*. For instance, in a LnO_6 environment, stretching or bending the Ln–O(1) deviates the length and angle of Ln–O(2). In this study, this drawback was solved by letting the ligand atoms unchanged while the Eu^{3+} was freely displaced. Therefore, we have used the derivation proposed in reference [28], highlighted in the equations S31, S32 and S33, where α_{ij} are the angles between the vectors considering the *i*-th and *j*-th ligands and F_i, F_j is the force along these ligands, respectively. We emphasize that $F_j \rightarrow 0$ when using an optimized geometry, thus, no deformation of the bonds is present, causing the vanish of the first term of the right-hand side of equation S33, stemming equation S35 from the combination of S33 and S34.

$$k_i^{ef} = -\sum_{j=1}^{N}\left(F_j \frac{d\cos\alpha_{ij}}{dx_i} + \frac{dF_j}{dx_i}\cos\alpha_{ij}\right) \quad (S33)$$

$$\frac{dF_j}{dx_i} = \frac{dF_j}{dx_j}\frac{dx_j}{dx_i} = -k_j \cos\alpha_{ij} \quad (S34)$$

$$k_i^{ef} = \sum_{j=1}^{N} k_j \cos^2\alpha_{ij} \quad (S35)$$

Employing the method of the equivalent bonds[28], we obtain the *k* values solving equation S35, where the k_i^{ef} was found as described in the sequence and α_{ij} was obtained through the calculation detailed in the supplementary note S2. The main difference of this work compared to the reported in reference [28] is assigned to the effect of the non-bonding atoms upon the supercell, and the extraction of the force constants from the Hellmann-Feynman theorem, instead of a routine mass-weighted hessian calculation. This adaptation opens new possibilities to a quick and low-cost computational procedure to calculate the effective constants since Hellmann-Feynman theorem is available at different source codes, such as MultiWFN[29]. In this sense, the proposed modifications are graphically highlighted in Fig S1.

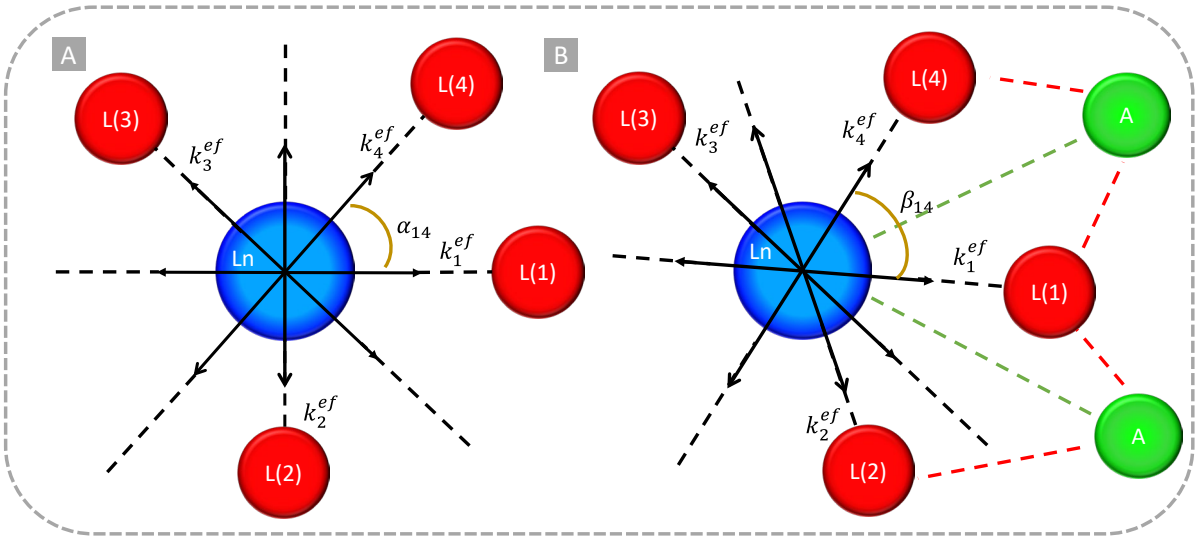

Fig S1. Schematic representative diagram for (a) the effective force constants of Ln^{3+} ion displacement in a six-coordinated site in a solid emphasizing the α_{14} angle, and (b) effective force constants emphasizing the β_{14} angle considering the non-bonding interaction of an atom A with the Ln (green dashed line) and with the ligand (red dashed line). Item (a) was adapted from reference 28.

The used parameters for the calculation described in the supplementary note S2 are summarized as follows. The bond overlap polarizability used for the calculations is listed in Table S2, the charge factors in Table S3, and the effective polarizability in Table S4.

Table S2. Calculated bond overlap polarizability values

Eu–O bond	Bond overlap polarizability (α_{OP}) / × 10^{-26} cm^2
Eu–O(1)	4.395
Eu–O(2)	4.732
Eu–O(3)	4.395
Eu–O(4)	4.056
Eu–O(5)	4.056
Eu–O(6)	4.731

Table S3. Calculated charge factors (g_j)

Film / %	Charge factor (g_j)					
	O(1)	**O(2)**	**O(3)**	**O(4)**	**O(5)**	**O(6)**
40	0.193	0.099	0.069	0.756	0.588	0.049
45	0.831	0.603	0.923	0.904	0.834	0.719
50	0.865	0.507	1.058	0.831	0.860	0.601
55	0.882	0.765	0.992	0.893	0.892	0.820
60	0.998	0.610	0.831	0.776	0.952	0.814
65	0.869	0.496	1.059	0.765	1.070	0.565
70	1.059	0.648	1.066	0.925	0.993	0.867

Table S4. Calculated effective polarizability from the fitting procedure (α')

Film / %	Effective polarizability (α') / Å^3					
	O(1)	O(2)	O(3)	O(4)	O(5)	O(6)
40	0.093	0.059	0.082	1.022	1.611	0.122
45	1.585	0.606	1.721	1.813	1.574	0.472
50	1.779	0.504	1.611	1.661	1.836	0.416
55	1.778	0.625	1.602	1.637	1.772	0.532
60	1.490	0.596	1.855	1.735	1.617	0.463
65	1.847	0.751	1.407	1.476	1.680	0.419
70	1.694	0.688	1.500	2.261	1.655	0.511

Force Constant Calculation using Hellmann-Feynman theorem

The calculation of the force constant was performed considering Eu–O bond as a diatomic-like molecule, under the influence of the indirect interaction of Eu^{3+} with the polymer matrix atoms. The forces were determined through the Hellmann-Feynman theorem within the adiabatic approximation, where the electrons follow the motion of atoms. Thus, the eigenvectors and eigenvalues {$|\Psi_n\rangle$ and E_n, respectively} are obtained as a consequence of the diagonalization of the Hamiltonian matrix[30]. The Hellmann-Feynman theorem states that if ψ_λ is a wavefunction of a Hamiltonian that depends on some parameter λ, that in this case is the stretching, and *E* is the eigenvalue of the Hamiltonian, then the derivative of the total energy with respect to the parameter relates with the expectation value of the derivative of the Hamiltonian with respect to the same parameter (equation S36). A derivation of the theorem is found in detail elsewhere[31]. For a fixed nuclear configuration under the Born-Oppenheimer approximation, the Schrödinger equation is rewritten in the form of equation S37, where the Hamiltonian is defined in expression S38.

$$\frac{dE}{d\lambda} = \langle\psi_\lambda|H|\psi_\lambda\rangle \quad (S36)$$

$$\hat{H}\psi_e = \left(\hat{T_e} + \hat{v}\right)\psi_e \quad (S37)$$

$$H = \hat{T_e} + \hat{V}_{ee} + \sum_{\alpha=1}^{M}\sum_{\beta>\alpha}^{M}\frac{Z_\alpha Z_\beta}{|R_\alpha - R_\beta|} - \sum_{i=1}^{N}\sum_{\alpha=1}^{M}\frac{Z_\alpha}{|r_i - R_\alpha|} \quad (S38)$$

In this case we emphasize the ionic part of the bonding since the Eu–O bonds possess a predominant ionic nature. Thus, considering a diatomic type, the *x*-component of the force acting on the nucleus (δ) is defined in equation S39, where the differentiation of the Hamiltonian considering normalized electronic wavefunction

results in equation S40. Although, including the covalency effects (with the spectral overlap) and the internuclear distances between Eu and O atoms, equation S41 is written, which its derivation can be found elsewhere[Error! Bookmark not defined.]. This form can be rewritten in the trigonometrical form model, allowing us to deal only with the bond angles (equation S42).

$$F_{X\delta} = -\frac{\partial E}{\partial X_\delta} = -\left\langle \psi_e \left| \frac{\partial H}{\partial X_\delta} \right| \psi_e \right\rangle \quad (S39)$$

$$F_{X\delta} = -\left\langle \psi_e \left| \sum_{i=1}^{N} \frac{x_i - X_\delta}{|r_i - R_\delta|^3} \right| \psi_e \right\rangle + Z_\delta \sum_{\alpha \neq \delta}^{M} Z_\alpha \frac{X_\alpha - X_\delta}{|R_\alpha - R_\delta|^3} \quad (S40)$$

$$F_{Ax} = -Z_A \left[\int \rho \frac{x_i - X_A}{|r_i - r_A|^3} dr_i - \frac{Z_B (X_B - X_A)}{|R_B - R_A|^3} \right] = -Z_A \left[\int \rho \frac{x_i - X_A}{r_{Ai}^3} dr_i - \frac{Z_B}{R^2} \right] \quad (S41)$$

$$F_{Ax} = -Z_A \int \rho \frac{cos\, \theta_{Ai}}{r_{Ai}^2} dr_i + \frac{Z_A Z_B}{R^2} \quad (S42)$$

The forces were directly used to determine the k_i^{ef} from the variation of the force acting on the *j*-th ligand altering the *i*-th ligand position, then, the effective force constant was used to obtain the overall k_j as described before in equation S35.

Supplementary Note S4 – Thermogravimetry and Derivative Thermogravimetry (TG and DTG)

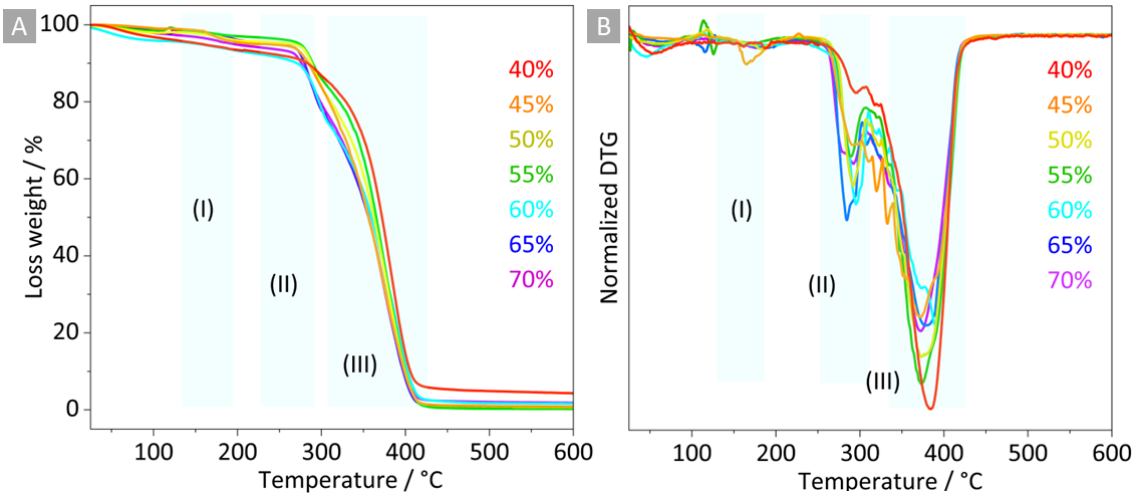

Fig S2. (a) TG curves for all films highlighting the three degradation steps (I), (II) and (III) at a 25 – 600 °C range and (b) DTG curves of all films

Table S5. Temperature range related to the peaks (I), (II), and (III) considering each process for all films, and the residue of each decomposition.

Film	Temperature range / °C			Weight loss / %			Residue / %
	(I)	(II)	(III)	(I)	(II)	(III)	
40%	148 – 216	259 – 309	322 – 421	5.84	15.5	73.7	38.7
45%	149 – 221	260 – 306	322 – 421	5.34	17.3	76.7	44.9
50%	150 – 219	263 – 309	325 – 422	3.41	14.0	73.2	48.9
55%	153 – 224	260 – 301	329 – 421	2.61	14.0	80.2	53.6
60%	152 – 218	264 – 304	324 – 422	3.40	12.8	80.6	61.2
65%	153 – 221	262 – 303	326 – 425	3.24	12.4	81.2	65.2
70%	154 – 218	264 – 301	329 – 426	3.05	12.1	81.7	69.6

Supplementary Note S5 – Morphological properties

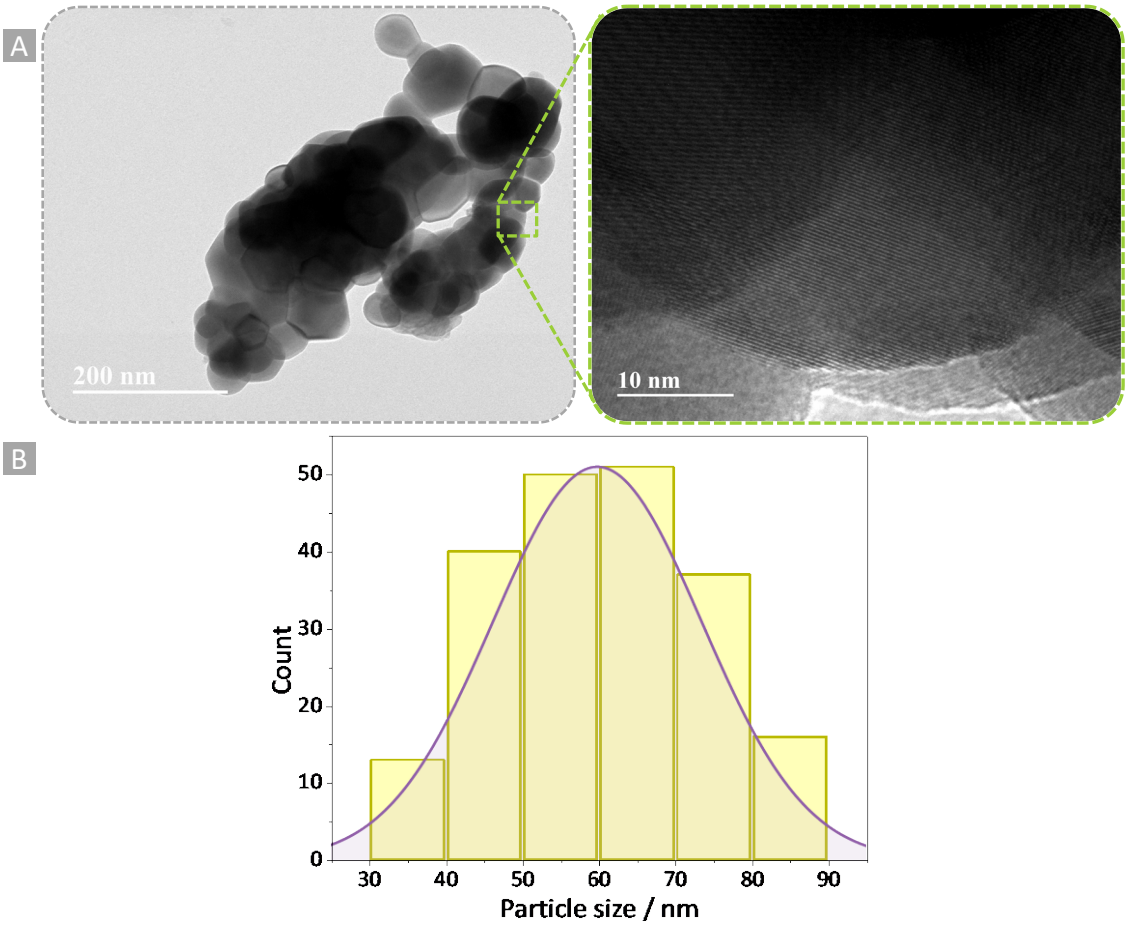

Fig S3. (a) TEM (200 nm scale) image and HRTEM (high resolution TEM) with magnification at 10 nm image of the SrY_2O_4:$Ce^{III/IV}$(2%),Eu^{III}(9%) phosphor. (b) Mean particle size histogram considering the analysis of a sample of 209 particles in five TEM images.

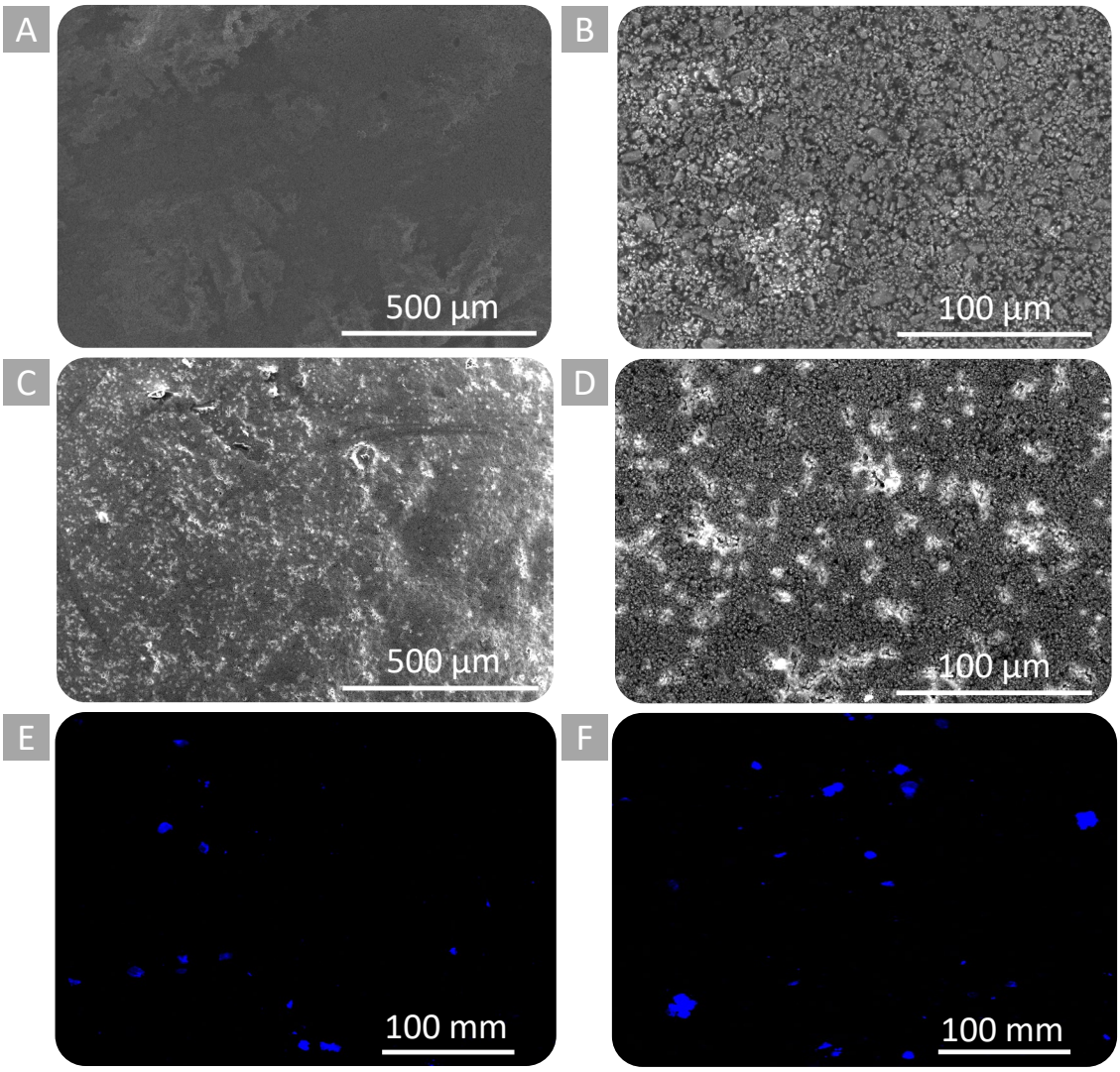

Fig S4. SEM images displaying the secondary electrons (SE) of the 40%-phosphor/film at (a) 100X magnification (b) 3000X magnification, and the 65%-phosphor/film at (c) 100X magnification, and (d) 3000X magnification. Images obtained by confocal microscopy of the (e) 40%-phosphor/film and (f) 65%-phosphor/film.

Supplementary note S6 – Structural analysis of the film

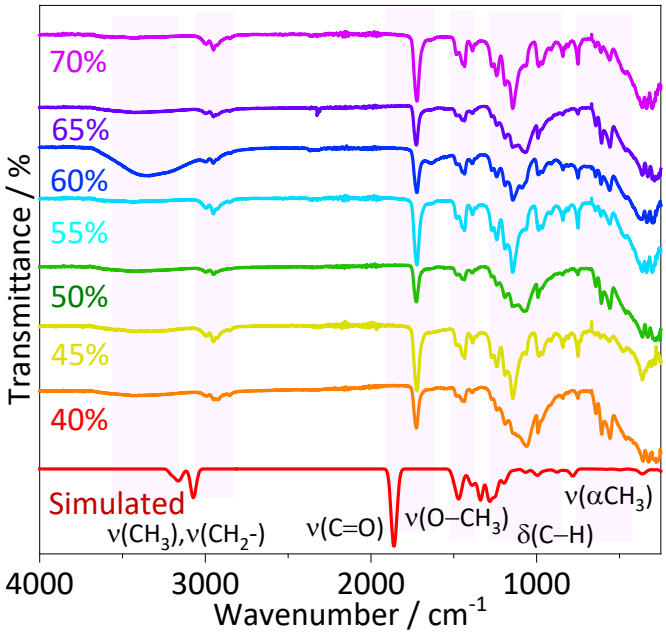

Fig S5. Full FTIR spectra at 250 – 4000 cm^{-1} range of all films

Table S6. Observed bands (cm^{-1}) in the IR spectra for all films and their assignments.

40%	45%	50%	55%	60%	65%	70%	Assignment
321	325	329	331	331	332	334	**ν(RE–O)**
461	465	466	468	470	471	474	**ν(RE–O)**
604	602	608	608	612	609	612	**ν(RE–O)**
749	749	754	750	750	749	754	**ν(αCH₃)**
988	984	992	990	993	992	992	**δ(C–H)**
1061	1061	1069	1069	1073	1073	1065	**ν(C–O–C)**
1245	1246	1242	1247	1241	1246	1248	**δ(O–H)**
1444	1442	1442	1440	1441	1436	1436	**ν(O–CH₃)**
1485	1486	1485	1489	1484	1481	1485	**δ(C–H)**
1727	1726	1729	1727	1725	1728	1727	**ν(C=O)**
2913	2919	2922	2928	2931	2937	2941	**ν(CH₂–)**
2998	2998	3002	3006	2999	3008	3012	**ν(CH₃)**
3396	3395	3398	3392	3396	3397	3399	**ν(O–H)**

Table S7. Observed bands (cm^{-1}) in Raman scattering spectra for all films and their assignments.

40%	45%	50%	55%	60%	65%	70%	Vibrational mode	Assignment
306	309	310	312	315	312	315	$B_{2g}(4)$	**M–O (M=Y^{3+},Sr^{2+})**
430	428	431	429	430	432	431	$A_{2g}(11)$	**M–O (M=Y^{3+},Sr^{2+})**
482	484	488	490	489	485	488	$A_{2g}(13)$	**M–O (M=Y^{3+},Sr^{2+})**
604	602	602	602	600	602	602	Symmetric stretching	**ν(C–CO)**
709	709	707	711	711	712	713	–	**Eu^{3+} ($^5D_0 \rightarrow {}^7F_3$)**
813	813	812	813	813	812	813	Rocking	**–CH_2**
998	1001	1002	1005	999	1002	1000	Rocking	**O–CH_3**
1259	1262	1263	1264	1264	1262	1262	Antisymmetric stretching	**ν(C–O)**
1454	1449	1452	1452	1447	1447	1452	Bending	**δ(O–CH_3)**
1660	1658	1662	1661	1660	1663	1661	Symmetric stretch	**ν(C=C)**
1701	1701	1701	1702	1702	1701	1071	–	**Eu^{3+} ($^5D_0 \rightarrow {}^7F_4$)**
1766	1768	1766	1767	1767	1767	1766	Symmetric stretch	**ν(C=O)**

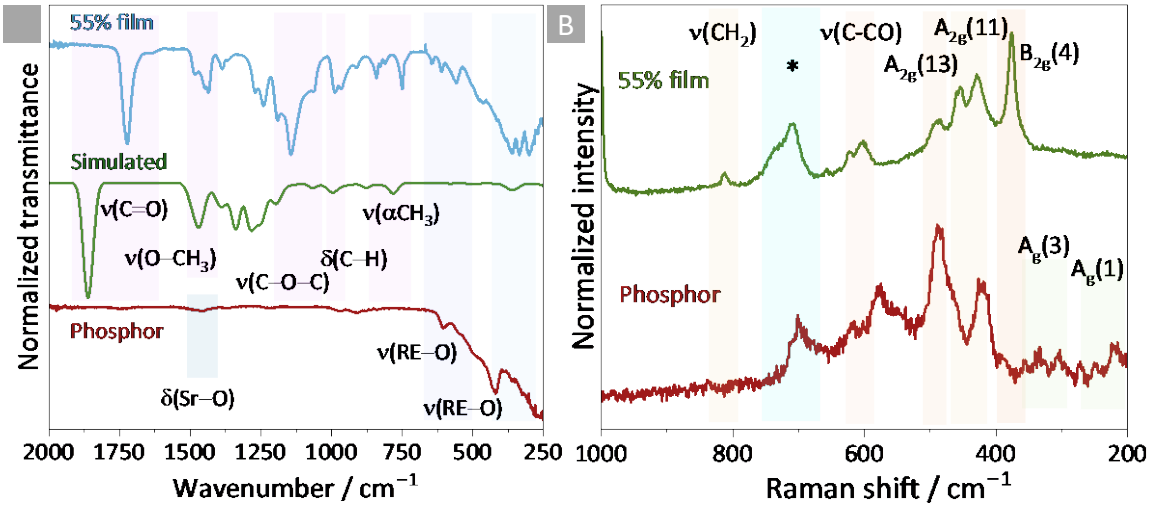

Fig S6. (a) FTIR spectrum of the 55% phosphor-film compared to the SrY_2O_4:$Ce^{III/IV}$(2%),Eu^{III}(9%) phosphor and the simulated FTIR of PMMA monomer using the ωB97x-3c/Def2-TZVP method, and (b) Raman spectrum of the 55% phosphor-film compared to the phosphor.

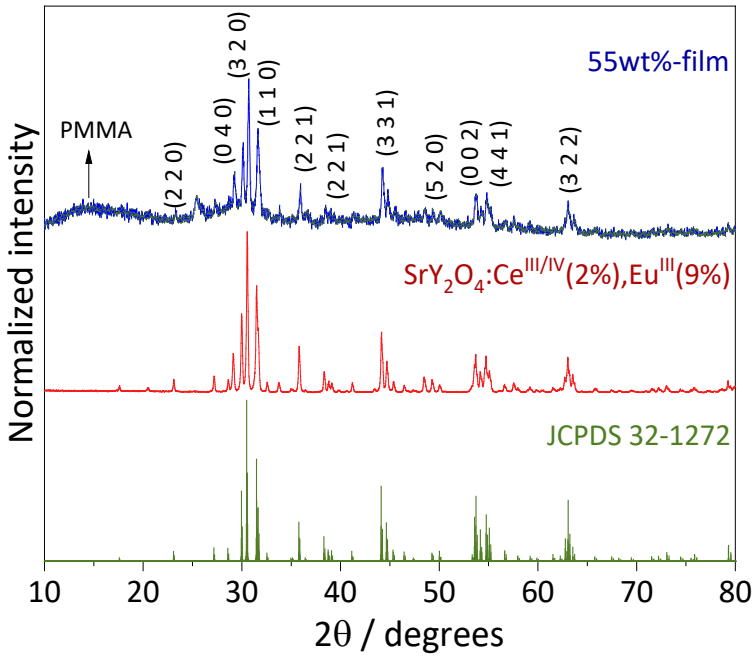

Fig S7. Powder X-ray diffraction patterns of the 55% phosphor-film compared to the $SrY_2O_4:Ce^{III/IV}(2\%),Eu^{III}(9\%)$ phosphor, where the Miller indices peaks are indexed to the JCPDS 32-1272 pattern. The halo ranging from 10 – 20 ° is assigned to the amorphous PMMA matrix, while the small peak in the 25° region is attributed to the tape used to hold the film in the sample holder of the equipment.

Supplementary note S7 – Optical bandgap

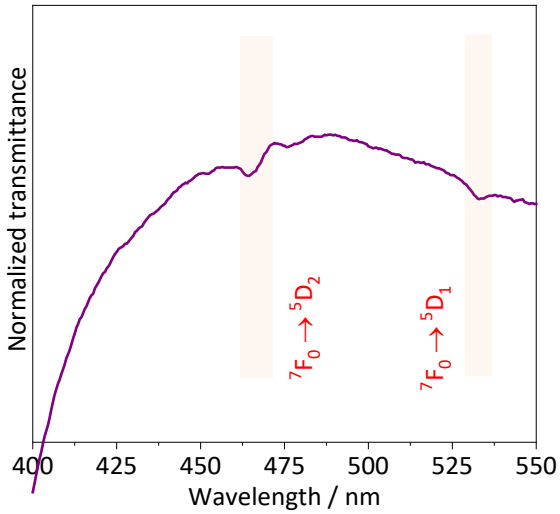

Fig S8. Amplified diffuse reflectance for the 60% phosphor/film composite highlighting the Eu^{III} *f-f* transitions.

The experimental optical bandgap of the bulk phosphor (Fig S6a) was calculated considering that the levels close to 3.5 eV are related to structural defects, as consequences of the Ln^{III}-dopants in the crystal. On the other hand, the optical bandgap of the undoped PMMA film was determined according to reference [32], in which the first band is assigned to the Urbach tail effects below 4 eV, and intra-band transitions below 4.5 eV.

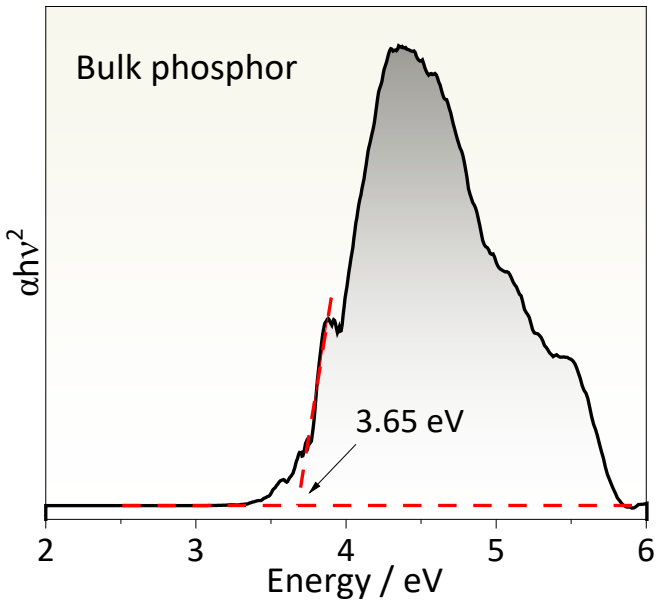

Fig S9. Bandgap determination from the DRS considering a direct transition in the bulk $SrY_2O_4:Ce^{III/IV},Eu^{III}$ phosphor.

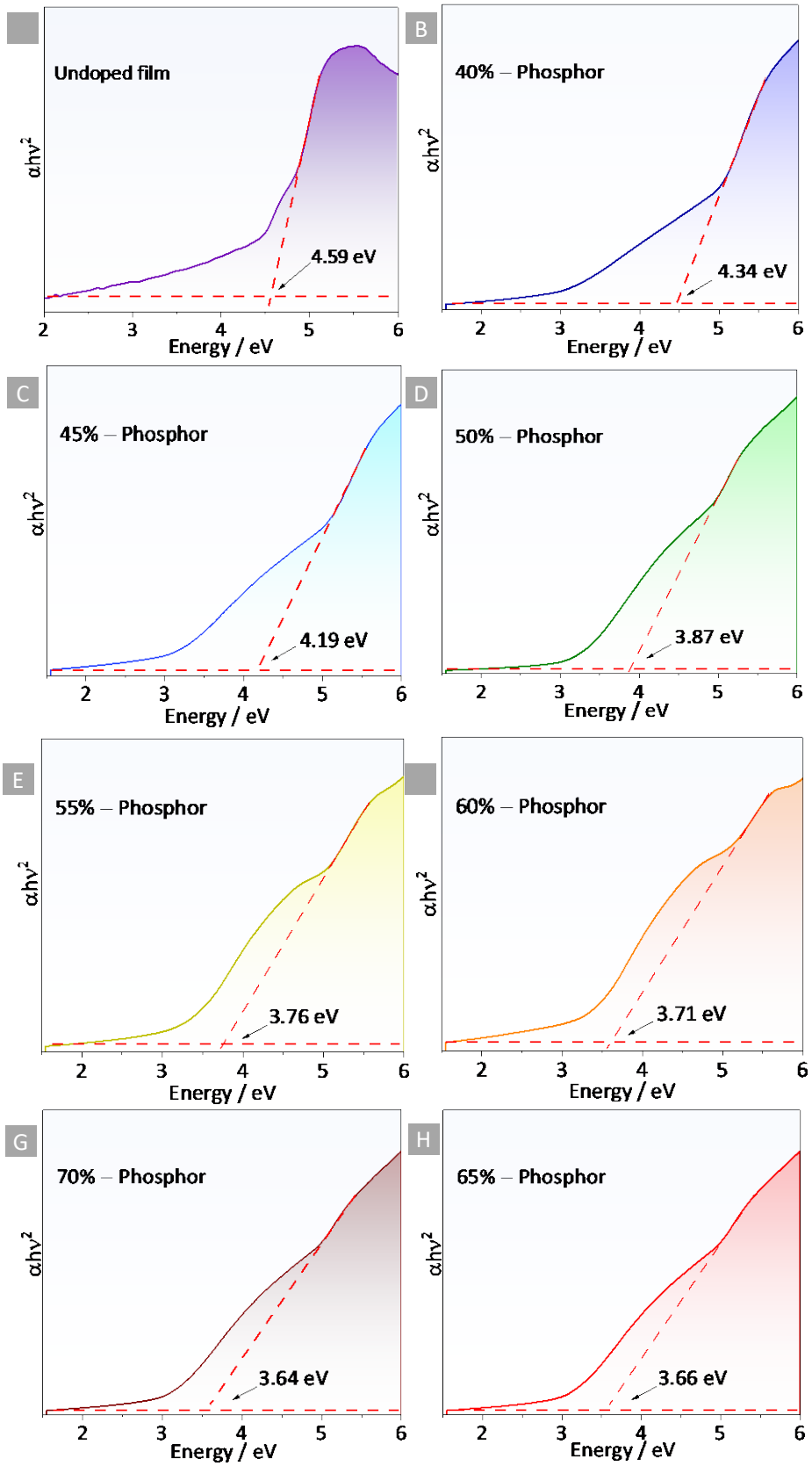

Fig S10. *Bandgap* calculation considering direct transition for the (a) undoped film, (b) 40/60% phosphor/PMMA, (c) 45/55% phosphor/PMMA, (d) 50/50% phosphor/PMMA, (e) 55/45% phosphor/PMMA, (f) 60/40% phosphor/PMMA, (g) 65/35 phosphor/PMMA and (h) 70/30% phosphor/PMMA.

Table S8. Optical band gap values for each film.

Film (phosphor/PMMA) %	Optical band gap / eV
Bulk phosphor	3.65
Undoped film	4.59
40/60	4.34
45/55	4.19
50/50	3.87
55/45	3.76
60/40	3.71
65/35	3.66
70/30	3.64

It is noteworthy that the particle size distribution (Fig S3b) yielded average values (56.4 nm) shorter than the wavelength range where the diffuse reflectance spectra was measured (200 – 800 nm), therefore, according to Rayleigh scattering theory, smaller wavelengths are much scattered than longer wavelengths. As the particle size increases (Fig S3b), higher intensities are found for the scattering, as a consequence of augmenting the volume as shown in equation S43, leading to lower transmittance in the UV region.[33] The fluctuation in the transmittance values can affect the measured bandgap, however, the desired agreement between the theoretical electronic bandgap and optical bandgap of the bulk phosphor and films implies the considerable consistence of the approach. In this equation, *k* is a proportional constant, V is the volume of the particle, *n* is the refractive index and $\boldsymbol{\varphi}$ is the scattering angle at position distance *R*.

$$\frac{I_s}{I_0} = \left[\frac{k_i}{n_0}\right]^4 V^2 \frac{sin^2\varphi}{16\pi^2 R^2}[n^2 - n_0^2]^2 \quad (S43)$$

Supplementary Note S8 – Results of the composite theoretical structural analysis

The calculation yielded the main phosphor-polymer interface, which coincides with the (0 0 1) lattice plane, as presented in Figure S8. Also, the optimization results are summarized in Table S8, and S9 – S16, where the first describes the number of neighbours and the nearest polymer groups of each europium atom in the supercell. The values in Table S9 – S16 are related to all bonds in the simulated composite, thus, C–H bonds refers to all the C–H in each functional group of the polymer. The same is seen for O–C and C–C. In the case of Metal–Oxygen bonds, only the first coordination sphere is considered, therefore, Eu–O, Ce–O, and Y–O describes only the bond length of the hexa-coordinated polyhedral, while Sr–O describes the bond length of the octa-coordinated polyhedral. For comparison purposes, the Metal-Metal distances do not characterize effective bonds, they are kept in the table in angstrom and with the same notation.

Table S9. Number of neighbours and nearest polymer groups of each europium atom in the supercell for the 55% phosphor/film.

$Atom_x$ (x = site)	Number of neighbors	Nearest polymer group
Eu_1	14	Ester
Eu_2	11	Methyl
Eu_3	11	Methyl
Eu_4	9	Tert-buthyl
Eu_5	14	Ester
Eu_6	11	Tert-buthyl
Eu_7	11	Methyl
Eu_8	9	Ester

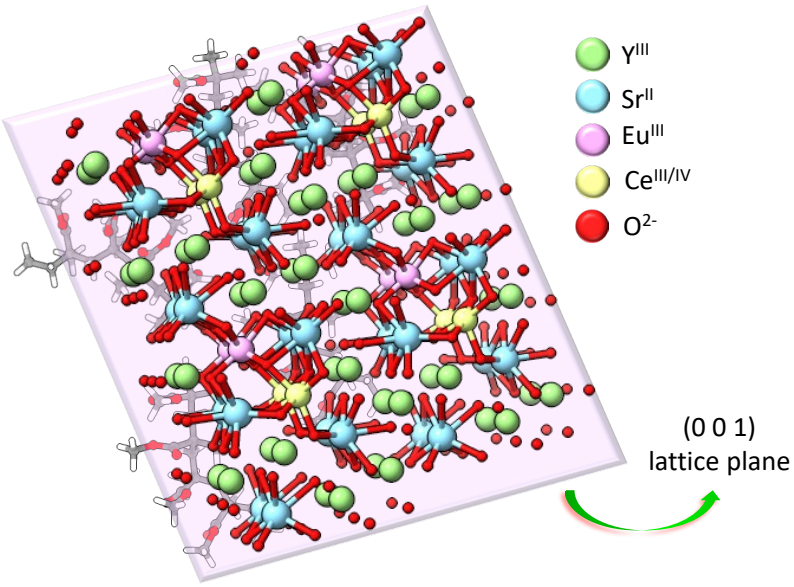

Fig S11. Position of the (0 0 1) lattice plane related to the phosphor-polymer interface. The most distant Eu^{III} atoms of the plane are considered as being in the "internal region" while the closest to the plane are considered as being in the interface.

Table S10. Distance between atoms with its minimum, average and maximum value in angstrom for the 40% Phosphor/PMMA film.

Bond	Minimum distance / Å	Average distance / Å	Maximum distance / Å
C–H	1.0815	1.0955	1.1775
C–C	1.5090	1.5454	1.5920
O–C	1.2093	1.3262	1.5486
Sr–H	2.1082	2.4628	2.7785
Sr–C	2.6873	3.0008	3.4099
Sr–O	1.9309	2.3630	3.2899
Sr–Sr	3.3599	3.9762	4.8151
Y–H	2.5110	2.5736	2.6363
Y–O	1.7991	2.1210	2.6327
Y–Sr	3.2172	3.9441	4.7494
Y–Y	3.3574	3.8599	4.5069
Ce–O	1.8806	2.2237	3.1955
Ce–Sr	3.2747	4.0028	4.8543
Ce–Y	3.2410	3.9262	4.5801
Ce–Ce	3.4097	3.5096	3.5737
Eu–O	2.2185	2.4268	2.6283
Eu–Sr	3.3424	3.9271	4.8281
Eu–Y	3.4150	4.0764	4.5869
Eu–Ce	3.9434	4.4997	4.6795
Eu–Eu	3.3650	3.5587	3.9705

Table S11. Distance between atoms with its minimum, average and maximum value in angstrom for the 45% Phosphor/PMMA film.

Bond	Minimum distance / Å	Average distance / Å	Maximum distance / Å
C–H	1.0821	1.0986	1.1975
C–C	1.5192	1.6454	1.6980
O–C	1.2193	1.3472	1.5546
Sr–H	2.1180	2.4688	2.7785
Sr–C	2.6973	3.0108	3.4189
Sr–O	1.9701	2.3730	3.2996
Sr–Sr	3.3499	3.8762	4.6151
Y–H	2.5110	2.5736	2.6363
Y–O	1.8891	2.2210	2.5327
Y–Sr	3.2172	3.9441	4.7494
Y–Y	3.3584	3.7519	4.2029
Ce–O	1.8106	2.2347	3.1955
Ce–Sr	3.2749	4.0021	4.8443
Ce–Y	3.2410	3.9262	4.5801
Ce–Ce	3.4097	3.5096	3.5737
Eu–O	2.1923	2.4658	2.6783
Eu–Sr	3.3424	3.9271	4.8281
Eu–Y	3.4150	4.0764	4.5869
Eu–Ce	3.9434	4.4997	4.6795
Eu–Eu	3.3450	3.5418	3.8405

Table S12. Distance between atoms with its minimum, average and maximum value in angstrom for the 50% Phosphor/PMMA film.

Bond	Minimum distance / Å	Average distance / Å	Maximum distance / Å
C–H	1.0815	1.0955	1.1775
C–C	1.5090	1.5454	1.5920
O–C	1.2093	1.3262	1.5486
Sr–H	2.1082	2.4628	2.7785
Sr–C	2.6873	3.0008	3.4099
Sr–O	1.9309	2.3630	3.2899
Sr–Sr	3.3599	3.9762	4.8151
Y–H	2.5110	2.5736	2.6363
Y–O	1.7991	2.1210	2.6327
Y–Sr	3.2172	3.9441	4.7494
Y–Y	3.3574	3.8599	4.5069
Ce–O	1.8806	2.2237	3.1955
Ce–Sr	3.2747	4.0028	4.8543
Ce–Y	3.2410	3.9262	4.5801
Ce–Ce	3.4097	3.5096	3.5737
Eu–O	2.2084	2.4439	2.6283
Eu–Sr	3.3424	3.9271	4.8281
Eu–Y	3.4150	4.0764	4.5869
Eu–Ce	3.9434	4.4997	4.6795
Eu–Eu	3.4106	3.5621	3.7699

Table S13. Distance between atoms with its minimum, average and maximum value in angstrom for the 55% Phosphor/PMMA film.

Bond	Minimum distance / Å	Average distance / Å	Maximum distance / Å
C–H	1.0825	1.0955	1.1775
C–C	1.5152	1.5828	1.6117
O–C	1.2141	1.3289	1.5574
Sr–H	2.1148	2.4638	2.8786
Sr–C	2.6783	3.1318	3.4189
Sr–O	2.0319	2.3672	2.9199
Sr–Sr	3.3487	3.9752	4.8104
Y–H	2.5314	2.5785	2.6562
Y–O	1.801	2.2106	2.6217
Y–Sr	3.2078	3.9541	4.7258
Y–Y	3.3451	3.8602	4.4598
Ce–O	1.8902	2.2307	3.2152
Ce–Sr	3.2841	4.0128	4.8558
Ce–Y	3.2405	3.9256	4.5902
Ce–Ce	3.4187	3.5209	3.5656
Eu–O	2.2509	2.4695	2.6332
Eu–Sr	3.3465	3.9381	4.8205
Eu–Y	3.4144	4.0752	4.6598
Eu–Ce	3.9521	4.4802	4.6851
Eu–Eu	3.4682	3.5109	3.8508

Table S14. Distance between atoms with its minimum, average and maximum value in angstrom for the 60% Phosphor/PMMA film.

Bond	Minimum distance / Å	Average distance / Å	Maximum distance / Å
C–H	1.0812	1.0854	1.7726
C–C	1.5192	1.5406	1.5912
O–C	1.2198	1.3165	1.5467
Sr–H	2.1181	2.4632	2.7895
Sr–C	2.6871	3.0121	3.4135
Sr–O	1.9308	2.3622	3.2884
Sr–Sr	3.3598	3.9754	4.8126
Y–H	2.5102	2.5742	2.6384
Y–O	1.7998	2.1523	2.6351
Y–Sr	3.2178	3.9456	4.7523
Y–Y	3.3571	3.8369	4.5024
Ce–O	1.8836	2.2289	3.1764
Ce–Sr	3.2741	4.0128	4.8568
Ce–Y	3.2412	3.9275	4.5803
Ce–Ce	3.4187	3.5248	3.5702
Eu–O	2.1589	2.3874	2.5298
Eu–Sr	3.3413	3.8702	4.6909
Eu–Y	3.4143	4.0892	4.5801
Eu–Ce	3.9502	4.9741	4.6598
Eu–Eu	3.3521	3.4492	3.5715

Table S15. Distance between atoms with its minimum, average and maximum value in angstrom for the 65% Phosphor/PMMA film.

Bond	Minimum distance / Å	Average distance / Å	Maximum distance / Å
C–H	1.0812	1.0921	1.1756
C–C	1.5084	1.5402	1.5867
O–C	1.2084	1.3161	1.5298
Sr–H	2.1107	2.4569	2.7784
Sr–C	2.6869	3.0456	3.4167
Sr–O	1.9322	2.3645	3.2904
Sr–Sr	3.3601	3.9754	4.8205
Y–H	2.5117	2.5784	2.6531
Y–O	1.8012	2.1132	2.6389
Y–Sr	3.2214	3.9456	4.7486
Y–Y	3.3402	3.8552	4.5061
Ce–O	1.8906	2.2304	3.1957
Ce–Sr	3.2751	4.0126	4.8542
Ce–Y	3.2409	3.9265	4.5903
Ce–Ce	3.4156	3.5184	3.5689
Eu–O	2.1909	2.3812	2.6256
Eu–Sr	3.3412	3.9237	4.8108
Eu–Y	3.4159	4.0786	4.5802
Eu–Ce	3.9485	4.4892	4.6804
Eu–Eu	3.4504	3.5297	3.6714

Table S16. Distance between atoms with its minimum, average and maximum value in angstrom for the 70% Phosphor/PMMA film.

Bond	Minimum distance / Å	Average distance / Å	Maximum distance / Å
C–H	1.0821	1.0923	1.1746
C–C	1.5092	1.4856	1.5982
O–C	1.2186	1.3268	1.5445
Sr–H	2.1073	2.4631	2.7795
Sr–C	2.6678	3.0108	3.4156
Sr–O	1.9399	2.3598	3.2897
Sr–Sr	3.3601	3.9741	4.8106
Y–H	2.5169	2.5784	2.6303
Y–O	1.8099	2.1207	2.6359
Y–Sr	3.2287	3.9405	4.7806
Y–Y	3.3581	3.8609	4.5109
Ce–O	1.8941	2.2256	3.1942
Ce–Sr	3.2759	4.0128	4.8542
Ce–Y	3.2456	3.9189	4.5904
Ce–Ce	3.4108	3.5175	3.5642
Eu–O	2.1589	2.3487	2.6752
Eu–Sr	3.3432	3.9706	4.8298
Eu–Y	3.4142	4.0768	4.5899
Eu–Ce	3.9411	4.4999	4.6798
Eu–Eu	3.3421	3.3891	3.5715

Table S17. Eu–O bond length for the phosphor according to previous work published by us [34], and the least and most neighbored Eu^{III} environment for the 55% film.

Eu–L(i) bond	Bond length / Å		
	Bulk phosphor	Least neighbored environment	Most neighbored environment
O(1)	2.306	2.294	2.284
O(2)	2.351	2.342	2.326
O(3)	2.306	2.296	2.288
O(4)	2.351	2.338	2.328
O(5)	2.426	2.411	2.402
O(6)	2.425	2.407	2.399
Eu	4.021	3.369	3.352

Supplementary note S9 – Photoluminescence and theoretical Judd-Ofelt parameters

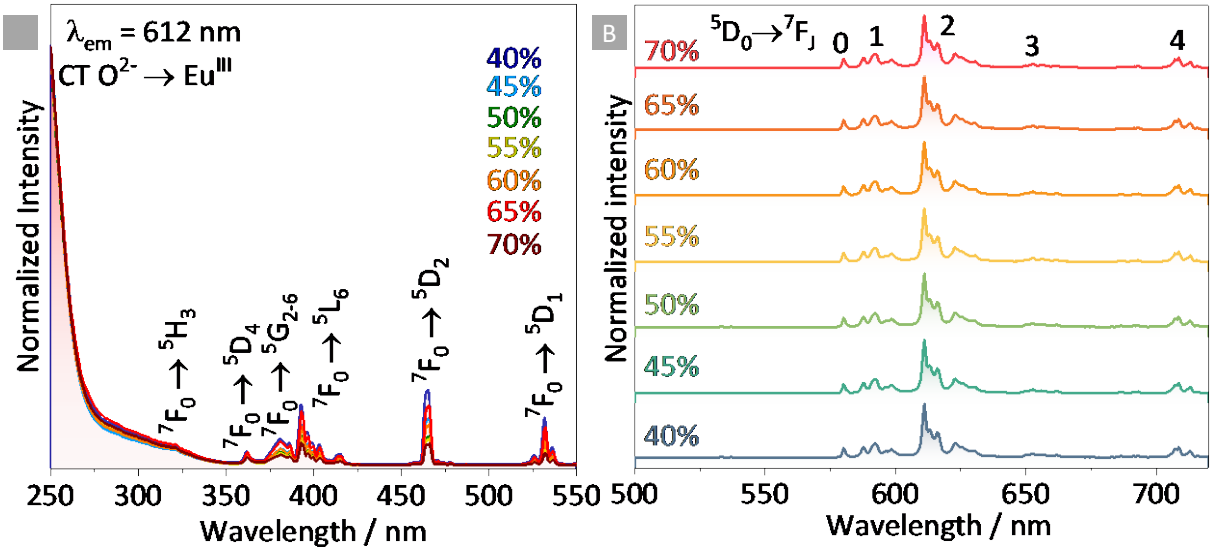

Fig S12. (a) Excitation spectra for all films and (b) emission spectra for all films recorded at 298 K, λ_{exc} = 394 nm.

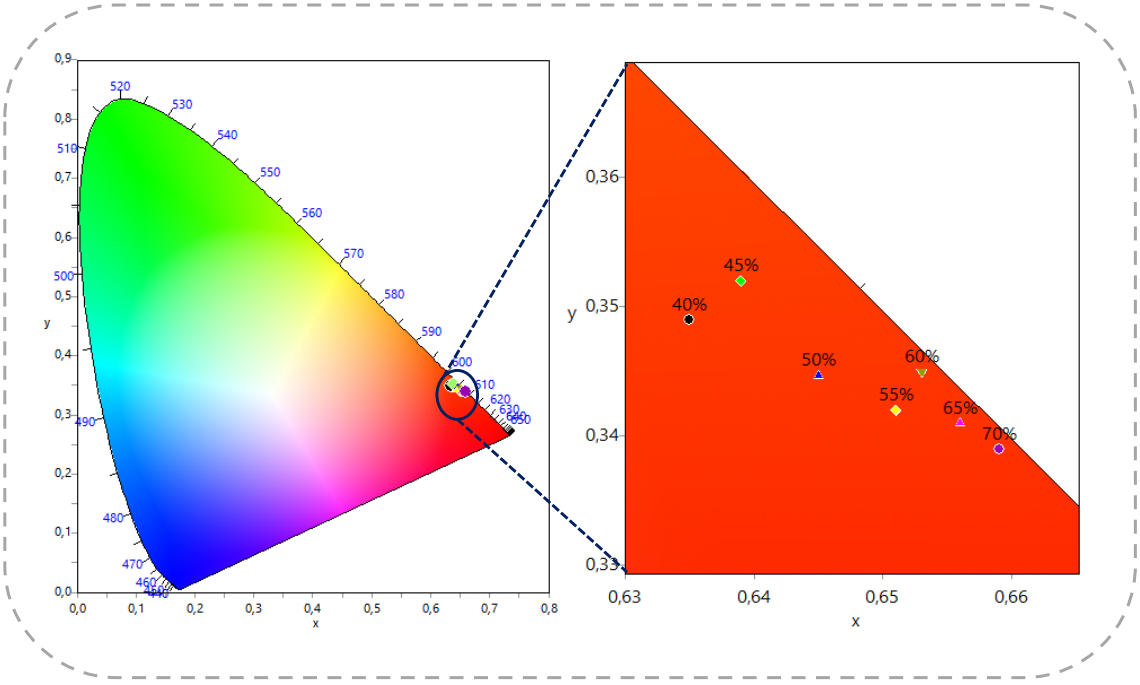

Fig S13. 1931 color chromaticity diagram (CIE) for all luminescent films

Table S18. CIE coordinates for all luminescent films

Phosphor / %	CIE coordinates	Color purity / %
40	(0.635; 0.349)	93.3
45	(0.639; 0.352)	94.4
50	(0.645; 0.344)	95.8
55	(0.651; 0.342)	96.0
60	(0.653; 0.345)	96.5
65	(0.659; 0.339)	97.8
70	(0.656; 0.341)	98.1

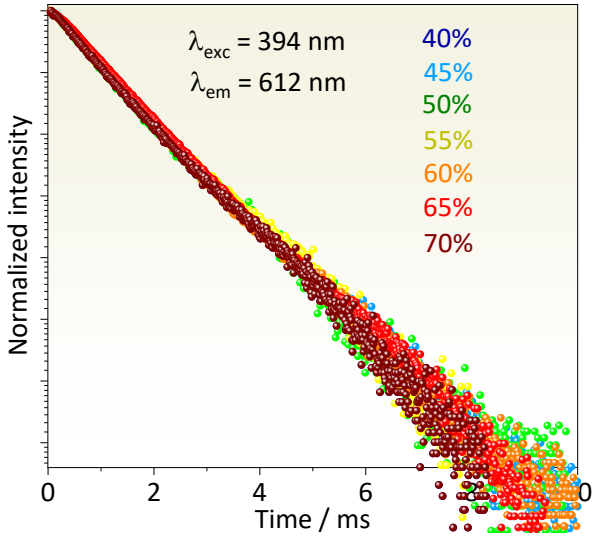

Fig S14. Emission decay curves at 298 K.

All calculations reported in the supplementary note S3 resulted in the contribution of the FED and DC mechanism, which are listed in Table S19.

Table S19. Calculated relative (%) contributions of the forced electric dipole (FED) alongside the dynamic coupling (DC) mechanism to the total theoretical intensity parameters, and the contribution of the bond overlap polarizability (α_{OP}) to the intensity parameters.

Film	% FED contribution		% DC contribution		α_{OP} contribution / %	
	Ω_2	Ω_4	Ω_2	Ω_4	Ω_2	Ω_4
40%	2.60	2.50	97.4	97.5	1.01	5.21
45%	1.30	4.70	98.7	95.3	0.99	2.09
50%	1.40	4.40	98.6	93.6	0.95	2.82
55%	1.60	6.00	98.4	94.0	1.04	3.54
60%	1.50	5.50	98.5	94.5	1.03	3.81
65%	1.70	4.20	98.3	95.8	1.08	4.54
70%	2.20	6.00	97.8	94.0	1.11	3.21

References

[1] S. P. Gorphade, R. H. Krishna, R. M. Melavanki, V. Dubey, N. R. Patil, Optik, 2020, 208, 164533.

[2] P. Kubelka, F. Munk, Ein Beitrag zur Optik der Farbanstriche, Z. Tech. Phys, (1931), 15, 593 – 601.

[3] A. G. Bispo-Jr, S. A. M. Lima, S. Lanfredi, F. R. Praxedes, A. M. Pires, J. Lumin, 2019, 214, 116604.

[4] W. T. Carnall, P. R. Fields, K. Rajnak, J. Chem. Phys, 1968, 49, 4450 – 4457.

[5] R. T. Moura Jr, M. Quintano, C. V. Santos Jr, V. A. C. A. Albuquerque, E. C. Aguiar, E. Kraka, A. N. C. Neto, Opt. Mat, 2022, 16, 100216.

[6] M. Müller, A. Hansen, S. Grimme, J. Chem. Phys, 2023, 158, 014103.

[7] P. Pracht, D. F. Grant, S. Grimme, J. Chem. Theory Comput, 2020, 16, 7044 – 7060.

[8] W. J. Hehre, R. F. Stewart, J. A. Pople, J. Chem. Phys, 1969, 51, 2657.

[9] C. Bannwarth, E. Caldeweyher, S. Ehlert, A. Hansen, P. Pracht, J. Seibert, S. Spicher, S. Grimme, WIREs Comput Mol Sci, 2021, 11, e1493.

[10] C. C. J. Roothaan, Rev. Modern Phys, 1951, 23, 69.

[11] G. G. Hall, Roy. Soc, 1951, 205.

[12] T. Bredow, G. Geudtner, K. Jug, J. Comp. Chem, 2001, 22, 89 – 101.

[13] Bannwarth, C.; Ehlert, S.; Grimme, S. J. Chem. Theory Comp, 2019, 15.

[14] A. B. Anderson, J. Chem. Phys, 1975, 62, 1187.

[15] K. Nishimoto, N. Mataga, Z. Phys. Chem, 1957, 12, 335 – 338.

[16] K. Ohno, Theor. Chim. Acta, 1964, 2, 219 – 227.

[17] G. Klopman, J. Am. Chem. Soc, 1964, 86, 4550 – 4557.

[18] S. Grimme, J. Antony, S. Ehrlich, H. Krieg, J. Chem. Phys, 2010, 132, 154104.

[19] E. Caldeweyher, S. Ehlert, A. Hansen, H. Neugebauer, S. Spicher, C. Bannwarth, S. Grimme, J. Chem. Phys, 2019, 150, 154122.

[20] A. M. Köster, M. Leboeuf, D. R. Salahub, in: Murray JS, Sen K, editors. Molecular electrostatic potentials. Theoretical and Computational Chemistry, 1996, vol. 3, pp. 105 – 142.

[21] M. Hülsen, A. Weigand, M. Dolg, Theor. Chem. Acc, 2009, 122, 23 – 29.

[22] G. F. de Sá, O. L. Malta, C. M. Donegá, A. M. Simas, R. L. Longo, P.A Santa-Cruz, E. F. da Silva Jr, Coord. Chem. Rev, 2000, 196, 165 – 195.

[23] O. L. Malta, Chem. Phys. Lett, 1982, 87, 27 – 29.

[24] R. T. Moura Jr, A. N. C. Neto, R. L. Longo, O. L. Malta, J. Lumin, 2016, 170, 420 – 430.

[25] R. T. Moura Jr, M. Quintano, C. V. Santos-Jr, V. C. A. Albuquerque, E. C. Aguiar, E. Kraka, A. N. C. Neto, Opt. Mat. X, 2022, 16, 100216.

[26] R. T. Moura Jr, A. N. Carneiro Neto, E. C. Aguiar, C. V. Santos-Jr, E. M. de Lima, W. M. Faustino, E. E. S. Teotonio, H. F. Brito, M. C. F. C. Felinto, R. A. S. Ferreira, L. D. Carlos, R. L. Longo, O. L. Malta, Opt. Mat. X, 2021, 11, 100080.

[27] A. N. C. Neto, R. T. Moura Jr, Chem. Phys. Lett, 2020, 757, 137884.

[28] A. Shyichuk, R. T. Moura-Jr, A. N. C. Neto, M. Runowski, M. S. Zarad, A. Szczeszak, S. Lis, O. L. Malta, J. Phys. Chem. C, 2016, 120, 28497 – 28508.

[29] T. Lu, F. Chen, J. Comp. Chem, 2012, 33, 580 – 592.

[30] G. P. Zhang, T. F. George, Phys. Rev. B, 2002, 66, 033110.

[31] V. P. Gupta, in: Principle and Applications of Quantum Chemistry, 2016, pp. 339 – 357.

[32] S. B. Azis, O. G. Abdullah, A. M. Hussein, H. M. Ahmed, Polymers, 2017, 9, 626.

[33] G. D. Patterson, P. J. Carroll, R. Stevens, J. Pol. Sci: Pol. Phys. Ed, 1983, 21, 613 – 623.

[34] L. F. Saraiva, A. G. Bispo-Jr, S. A. M. Lima, A. M. Pires, J. Alloys and Comp, 2023, 938, 168595.